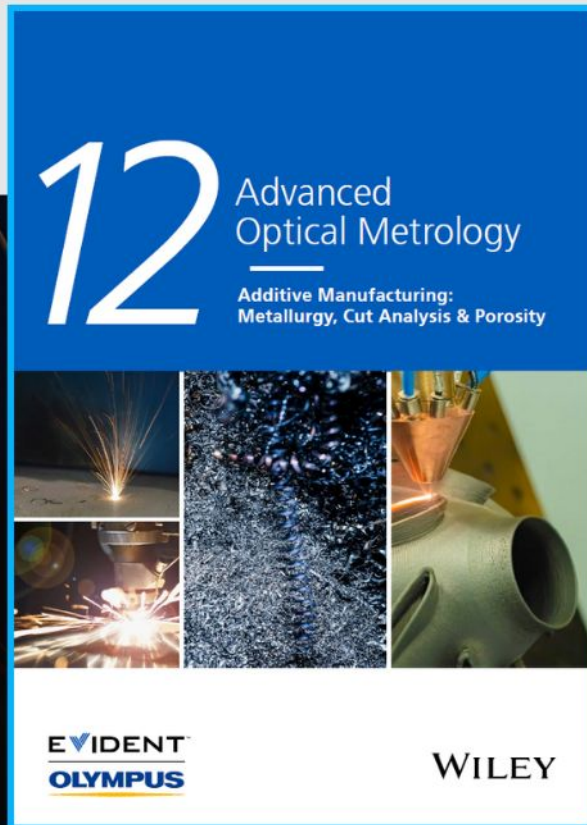




Additive Manufacturing: Metallurgy, Cut Analysis & Porosity

The latest eBook from
Advanced Optical Metrology.
Download for free.



In industry, sector after sector is moving away from conventional production methods to additive manufacturing, a technology that has been recommended for substantial research investment.

Download the latest eBook to read about the applications, trends, opportunities, and challenges around this process, and how it has been adapted to different industrial sectors.

EVIDENT
OLYMPUS

WILEY

Multifunction-Harnessed Afterglow Nanosensor for Molecular Imaging of Acute Kidney Injury In Vivo

Tikum Florence Anjong, Honghwan Choi, Joungyun Yoo, Yecheol Bak, Yuri Cho, Dojin Kim, Seokyoung Lee, Kangwon Lee, Bong-Gi Kim,* and Sehoon Kim*

Afterglow is superior to other optical modalities for biomedical applications in that it can exclude the autofluorescence background. Nevertheless, afterglow has rarely been applied to the high-contrast “off-to-on” activatable sensing scheme because the complicated afterglow systems hamper the additional inclusion of sensory functions while preserving the afterglow luminescence. Herein, a simple formulation of a multifunctional components-incorporated afterglow nanosensor (MANS) is developed for the superoxide-responsive activatable afterglow imaging of cisplatin-induced kidney injury. A multifunctional iridium complex (Ir-OTf) is designed to recover its photoactivities (phosphorescence and the ability of singlet oxygen-generating afterglow initiator) upon exposure to superoxide. To construct the nanoscopic afterglow detection system (MANS), Ir-OTf is incorporated with another multifunctional molecule (rubrene) in the polymeric micellar nanoparticle, where rubrene also plays dual roles as an afterglow substrate and a luminophore. The multiple functions covered by Ir-OTf and rubrene renders the composition of MANS quite simple, which exhibits superoxide-responsive “off-to-on” activatable afterglow luminescence for periods longer than 11 min after the termination of pre-excitation. Finally, MANS is successfully applied to the molecular imaging of cisplatin-induced kidney injury with activatable afterglow signals responsive to pathologically overproduced superoxide in a mouse model without autofluorescence background.

1. Introduction


Afterglow is a phenomenon in which a long-lasting emission without maintaining photoexcitation occurs as a result of the slow release of photons from a pre-excited material. Recently,

afterglow has emerged as a new promising modality for optical imaging in that it can exclude most of autofluorescence background by eliminating excitation during imaging, while maintaining the advantages of optical modality, such as the simplicity and non-invasive nature with high specificity and sensitivity.^[1–3]

Various mechanisms for the afterglow phenomenon have been proposed according to the constitution of materials, such as inorganics consisting of long persistent phosphors^[4–8] and organic nanoparticles containing semiconducting polymers or dyes using electron or energy transfer.^[9–18] Persistent luminescence from inorganic afterglow materials is attributed to the gradual release of energy from trap states with long decay times based on thermal stimulation, a phenomenon commonly referred to as thermally stimulated recombination. Conversely, several different mechanisms have been proposed for organic materials: 1) delay of excited electrons from reaching the ground state through a nonradiative intersystem crossing (ISC), known as organic ultra-long, room temperature phosphorescence

(OURTP);^[9,10,19–21] 2) reversed intersystem crossing (RISC) from the triplet to excited singlet states, such as thermally activated delayed fluorescence (TADF);^[22–24] or 3) chemiluminescence through the design of the relaxation pathway incorporating afterglow initiators, substrates, and relay units.^[11–16]

T. F. Anjong, H. Choi, J. Yoo, Y. Bak, Y. Cho, D. Kim, S. Lee, S. Kim
Center for Theragnosis
Korea Institute of Science and Technology
Seoul 02792, Republic of Korea
E-mail: sehoonkim@kist.re.kr

 The ORCID identification number(s) for the author(s) of this article can be found under <https://doi.org/10.1002/sml.202200245>.

© 2022 The Authors. Small published by Wiley-VCH GmbH. This is an open access article under the terms of the Creative Commons Attribution-NonCommercial-NoDerivs License, which permits use and distribution in any medium, provided the original work is properly cited, the use is non-commercial and no modifications or adaptations are made.

DOI: 10.1002/sml.202200245

H. Choi, B.-G. Kim
Department of Organic and Nano System Engineering
Konkuk University
Seoul 05029, Republic of Korea
E-mail: bgkim2015@konkuk.ac.kr

Y. Bak, K. Lee
Department of Applied Bioengineering
Graduate School of Convergence Science and Technology
Seoul National University
Seoul 08826, Republic of Korea

Y. Cho, S. Kim
KU-KIST Graduate School of Converging Science and Technology
Korea University
Seoul 02841, Republic of Korea

Among the advantages of optical imaging is the feasibility of using “off-to-on” activatable signals by elaborately designing the imaging agent as a disease-specific chemosensor, which is superior to “always-on” probes in terms of the diagnostic accuracy for molecular imaging.^[25,26] In the case of afterglow luminescence, however, “off-to-on” activatable signaling has rarely been attempted, presumably because most of afterglow systems are quite complex, which hampers the additional inclusion of sensory functions while preserving long-lasting luminescence in the biological environment.^[9,14,15] For this reason, afterglow imaging has mostly relied on “always-on” signals that inevitably generate nonspecific background noises from the miss-targeted probes, to compromise merits of the background-free afterglow modality. Recently, a chemiluminescence-based “off-to-on” afterglow probe responsive to hydrogen sulfide has been reported for the visualization of orthotopic liver tumor,^[16] proving the possible use of afterglow materials as an activatable bioprobe for diagnostic imaging in vivo. However, it relied on a complex nanoformulation composed of a number of ingredients with different roles (i.e., afterglow initiator, substrate, luminophore, and luminescence quencher). To expand the practical potential of “off-to-on” afterglow imaging, designing a simple composition of highly reliable and reproducible probes still remains a challenge. In this regard, harnessing multifunctional components that play diverse roles will provide a plausible and straightforward way to simplify the probe composition.

In order to incorporate multiple functions in a single molecular framework, we herein designed an iridium (III) complex that is intended to play dual roles of chemosensor and afterglow initiator. Iridium (III) complexes are among representative organometallic compounds that exhibit characteristic phosphorescence emission by the strong spin-orbit coupling-induced efficient intersystem crossing.^[27,28] With advantages, such as large stock shifts, high-phosphorescent efficiency, high photostability, and long-triplet lifetimes,^[29–31] they have been successfully applied to optical imaging as an “always-on” bioprobe.^[32–37] Iridium (III) complexes have also been explored as an “off-to-on” chemosensor for biosensing and activatable imaging applications.^[25,38] In addition to phosphorescence signaling, its long-lived triplet state allows for the production of singlet oxygen,^[39,40] thus suggesting its potential as an afterglow initiator capable of singlet oxygen (¹O₂)-mediated oxidation of afterglow substrate in the chemiluminescence mechanism. By virtue of such versatility, iridium complexes are considered as a promising candidate for constructing the multifunctional molecular framework.

In this study, a multifunctional iridium complex (Ir-OTf) was developed and rationally formulated with another multiple role molecule, rubrene, to produce a multifunction-harnessed afterglow nanosensor (MANS) for visualizing cisplatin-induced acute kidney injury (AKI) with activatable afterglow signals. Ir-OTf was designed as a chemosensor probe that performs: 1) sensing of endogenous superoxide (O₂^{·-}), one of reactive oxygen species (ROS) overproduced in injured/inflamed tissues, and then triggers the uncaging reaction to turn on its multiple photoactivities; that is, 2) ¹O₂ generation for afterglow initiation; and 3) phosphorescence emission for afterglow signaling. Co-formulated rubrene plays other dual roles for afterglow, that is: as 1) an afterglow substrate that reacts with photogenerated ¹O₂

and stores its energy in the form of dioxetane by chemical conversion; and 2) an additional afterglow emitter that can accept and harvest the Ir-OTf phosphorescence into longer-wavelength fluorescence by the intraparticle energy transfer. As a molecular probe, Ir-OTf was shown to have high selectivity and sensitivity to O₂^{·-} with no significant interference from other ROS, and thus by itself, potentiated activatable phosphorescence imaging of endogenous O₂^{·-} in vitro and ex vivo under photoexcitation. With its additional functionality (¹O₂ generation) and minimal toxicity, Ir-OTf was nanoformulated with rubrene into a simple two-component afterglow nanosensor system (MANS) and successfully applied to activatable afterglow imaging of O₂^{·-} overproduced in the injured kidney tissue of an AKI mouse model by in situ pre-excitation, demonstrating potential of the background-free afterglow signal for diagnostic imaging in vivo.

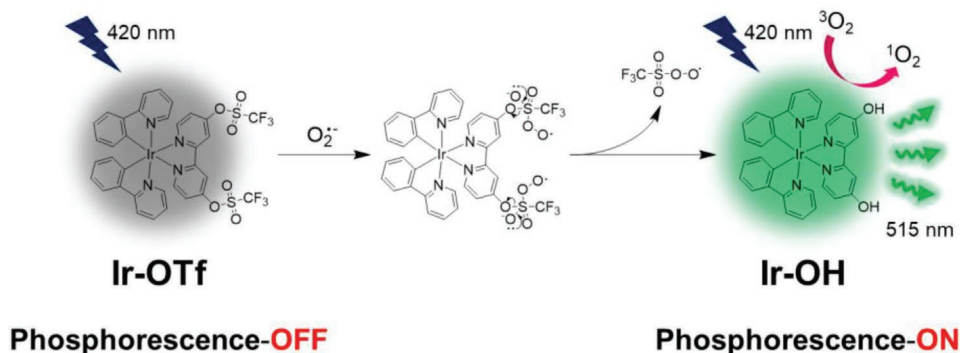
2. Results and Discussions

2.1. O₂^{·-}-Responsive Activatable Iridium Complex

Ir-OTf was synthesized by triflate protection of a hydroxyl iridium complex (Ir-OH) with trifluoromethanesulfonic anhydride (Scheme S1 and Figures S1 and S2, Supporting Information). The unprotected iridium complex (Ir-OH) is phosphorescent (Figure S3a, Supporting Information) and capable of generating ¹O₂ (Figure S3b, Supporting Information), while triflate protection was found to successfully quench its phosphorescence (Figure S3a, Supporting Information). Upon exposure to nucleophilic O₂^{·-}, the strong electron-withdrawing triflate group is susceptible to nucleophilic attack and capable of uncaging.^[41] Accordingly, Ir-OTf is designed to respond to O₂^{·-} by recovering the phosphorescence of Ir-OH, being an off-to-on phosphorogenic chemosensor for O₂^{·-} (Scheme 1). The absorption spectrum taken in PBS showed a high-energy band at <300 nm and a low-energy band in the range of 320–430 nm (Figure S3c, Supporting Information), which are assigned to the π–π* intraligand transition of the cyclometalating ligand and the d–π* metal-to-ligand charge transfer (MLCT), respectively.^[42]

To examine the selectivity of Ir-OTf toward O₂^{·-} in physiological environment, the phosphorogenic response was measured after adding various types of analytes, including physiological oxidants and reductants. As shown in Figure 1a,b, the quenched phosphorescence of Ir-OTf was recovered in response to O₂^{·-} and ONOO⁻ among other analytes. However, the phosphorescence response to O₂^{·-} was 2.6 times higher than that to ONOO⁻. It is also known that the physiological concentrations of O₂^{·-} and ONOO⁻ are also closely correlated with each other,^[43] thus concluding that the selectivity of Ir-OTf for O₂^{·-} detection is fairly high without significant interference from other physiological analytes. It was also confirmed that the sensing reaction kinetics of Ir-OTf is very fast to reach the saturated phosphorogenic intensity within a few seconds (Figure S4, Supporting Information).

The sensitivity of Ir-OTf to O₂^{·-} was further evaluated with varying amounts of O₂^{·-}. In the absence of O₂^{·-}, Ir-OTf showed only a weak phosphorescent emission at 565 nm (QY = 0.01, excited at 420 nm), whereas the emission intensity was increased in



Scheme 1. Molecular structure of Ir-OTf and its phosphorescence activation by $O_2^{\cdot-}$.

proportion to the concentration of $O_2^{\cdot-}$ (QY = 0.30 at 30 μM KO₂ with a peak shift to 515 nm) (Figure S5, Supporting Information). The phosphorescence intensity presented a linear correlation with the $O_2^{\cdot-}$ concentration in the examined range (Figure 1c). The limit of detection (LOD) was estimated to be 0.16 μM (using the 3σ method), which is comparable to other in vivo phosphorescent probes.^[44] Furthermore, the $O_2^{\cdot-}$ detection by Ir-OTf was stably performed in a wide pH range (<pH 9.0; Figure S6, Supporting Information), indicating the potential of Ir-OTf for sensing of $O_2^{\cdot-}$ in physiological environments. According to our probe design (Scheme 1), Ir-OTf is supposed to release triflate through the nucleophilic addition of $O_2^{\cdot-}$. Indeed, a peak corresponding to Ir-OH ($m/z = 687.0793$) was identified in the mass spectra of the sensing reaction product (Figure S7, Supporting Information), which is in good agreement with the proposed mechanism. Taken together, it was concluded that the sensing reaction of Ir-OTf with $O_2^{\cdot-}$ recovers optically active Ir-OH that is phosphorescent as well as capable of generating 1O_2 .

2.2. Phosphorogenic Detection of Endogenous $O_2^{\cdot-}$ in AKI Models by Ir-OTf

Cisplatin is one of the well-known chemotherapeutic drugs for the treatment of various types of cancer, such as testicular, ovarian, cervical, breast, and head and neck. Despite its notable anticancer effects, however, the risk of nephrotoxicity and hepatotoxicity caused by cisplatin has limited its uses.^[44] Reports

have shown that more than 10% of patients treated with cisplatin suffered from AKI,^[45] thus necessitating monitoring of drug-induced AKI for cisplatin treatments. Recently, $O_2^{\cdot-}$ has drawn considerable attention as a biomarker for the cisplatin-induced AKI.^[46,47] When cisplatin is introduced in the body, it undergoes metabolic activation in the renal epithelial cells^[48] and its active form affects the cellular antioxidant system by decreasing the levels of antioxidant protectors, such as superoxide dismutase, catalase, and glutathione peroxide, finally leading to an increase in the level of $O_2^{\cdot-}$ in the system.^[49]

To evaluate whether Ir-OTf is applicable to diagnostic imaging of AKI, its activatable chemosensor performance was first examined in vitro by photoluminescent monitoring of endogenously produced $O_2^{\cdot-}$ in a cisplatin-induced live cell model. To this end, HEK 293 cells were treated with different concentrations of cisplatin (0–1000 μM) for 12 h and subjected to Ir-OTf staining for 30 min. Under microscopic observation, unstimulated normal cells yielded dim phosphorescence, whereas the intracellular signal was gradually intensified with increasing the treating dose of cisplatin (Figure 2a and Figure S8, Supporting Information). Also, it was confirmed that almost no phosphorescence was observed in HEK 293 cells treated only with cisplatin without Ir-OTf (Figure S9, Supporting Information). To confirm that the observed phosphorogenic response of Ir-OTf is ascribed to the cisplatin-induced production of endogenous $O_2^{\cdot-}$, cells were pretreated with L-carnitine before treatment with cisplatin and Ir-OTf. L-carnitine is an amino acid-derived nutrient crucial for cellular energy management and its deficiency is known as

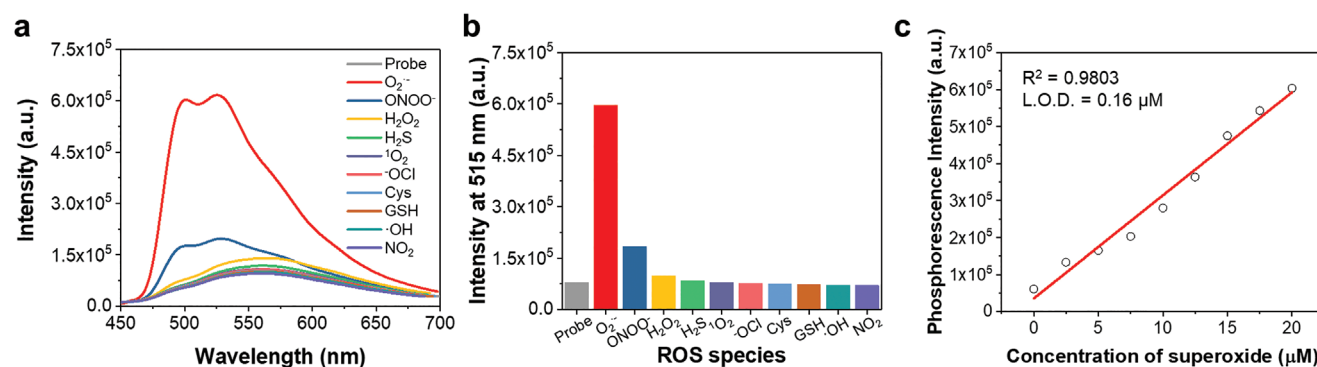


Figure 1. a) Phosphorescence spectra and b) histogram of phosphorescence intensities at 515 nm of Ir-OTf in the presence of various types of analytes in PBS (pH 7.4) (λ_{ex} : 420 nm). c) Phosphorescence intensity of Ir-OTf as a function of the $O_2^{\cdot-}$ concentration (λ_{ex} : 420 nm, λ_{em} : 515 nm).

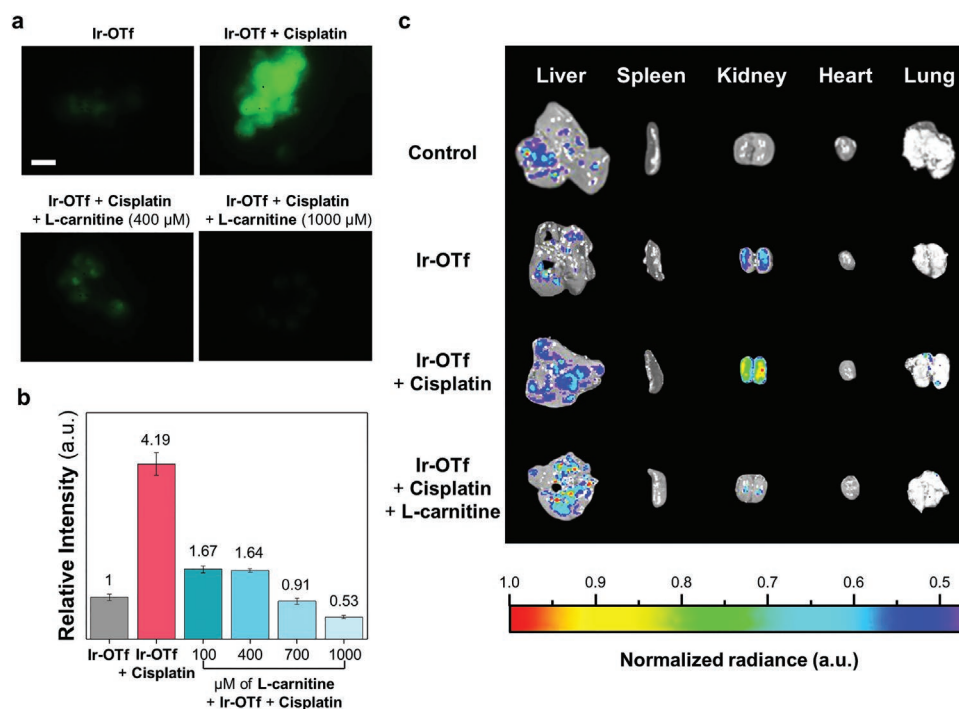


Figure 2. a) Phosphorescence images (λ_{ex} : 425 nm; λ_{em} : 500–600 nm) and b) histogram of relative phosphorescence intensities of Ir-OTf in HEK 293 cells. Cells were pre-incubated with or without L-carnitine and cisplatin (1000 μM) for 12 h, and then treated with Ir-OTf (10 μM) for 30 min. The data are presented as mean \pm standard error of the mean (SEM) ($n > 30$). Scale bar: 20 μm . c) Normalized ex vivo phosphorescence images of major organs resected 45 min after intravenous injection with Ir-OTf (0.95 mg kg^{-1}). Mice were pre-injected with PBS, cisplatin (20 mg kg^{-1}), or cisplatin with L-carnitine (500 mg kg^{-1}) 48 h before Ir-OTf injection.

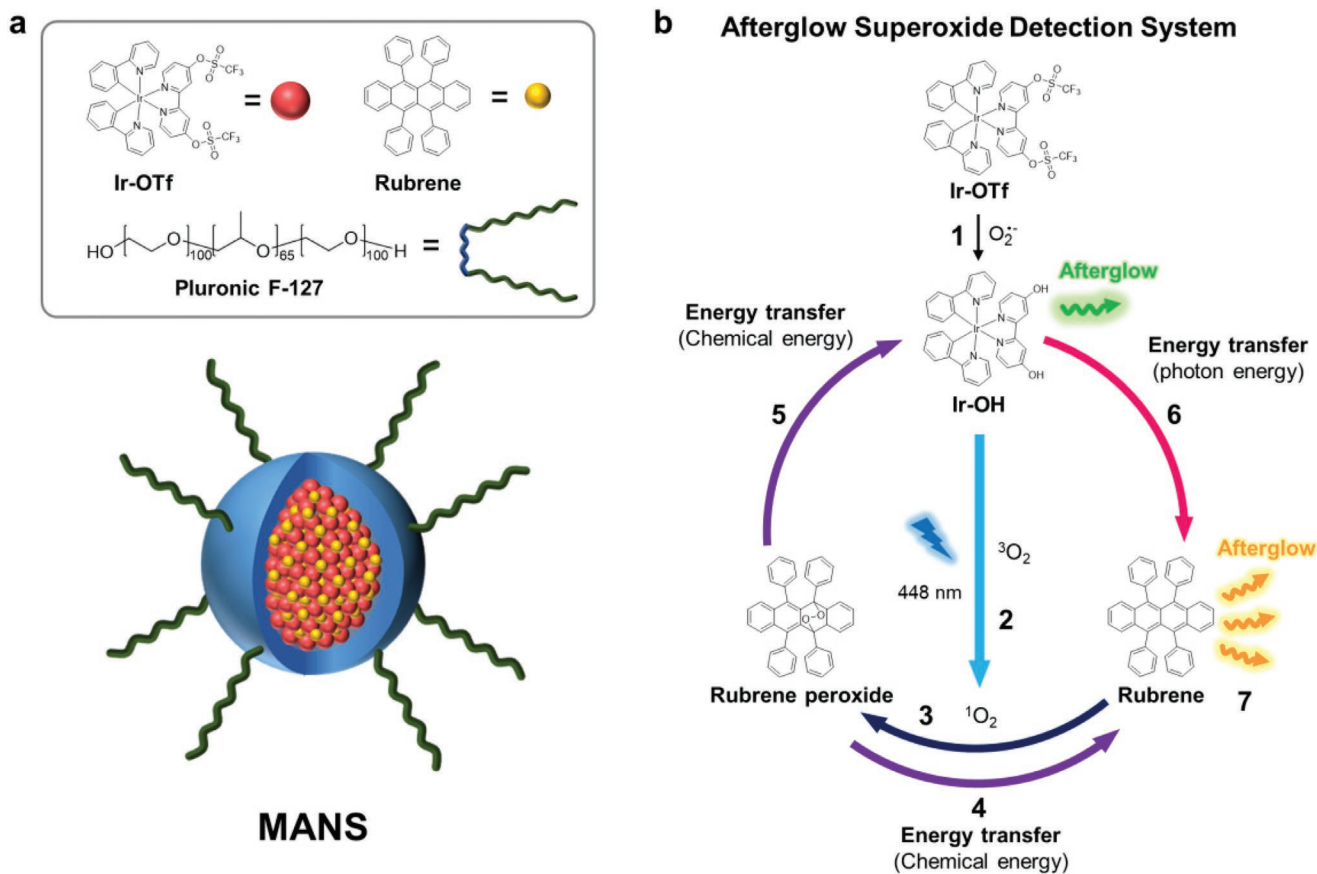
a causative factor in the development of kidney disease.^[50] It is reported that L-carnitine protects against cisplatin-induced oxidative stress by decreasing the level of lipid peroxidase (MDA) and elevates the activity of glutathione (GSH), glutathione-S-transferase (GST), and superoxide dismutase (SOD).^[51] As shown in Figure 2a,b, the phosphorogenic response to $\text{O}_2^{\cdot-}$ was notably reduced depending on the concentration of L-carnitine (0–1000 μM). These results support that a high level of $\text{O}_2^{\cdot-}$ is produced by the cisplatin-induced injury of kidney cells, and that L-carnitine can play a role in relieving it.

Subsequently, Ir-OTf was applied to the mouse model of AKI that was induced by intraperitoneal injection cisplatin (20 mg kg^{-1}). The AKI induction was histologically confirmed by hematoxylin and eosin (H&E) staining of the kidney tissue, where severe tubular and glomerular degenerative damages were observed 2–3 d after cisplatin administration (Figure S10, Supporting Information). The established mouse models were intravenously injected with Ir-OTf (0.95 mg kg^{-1}) and sacrificed after 45 min for the ex vivo imaging (Figure 2c). Compared to the normal control group, cisplatin-treated AKI mice yielded considerably enhanced phosphorescence signals of Ir-OTf selectively in the kidney among other organs, indicating the overproduction of $\text{O}_2^{\cdot-}$ by the injury of kidney cells. Similar to the in vitro observation, L-carnitine diminished the $\text{O}_2^{\cdot-}$ -activated kidney signal significantly when administered intraperitoneally prior to cisplatin treatment, implying that it could protect the kidney tissue from injury by preventing the production of $\text{O}_2^{\cdot-}$. Indeed, the histological examination revealed that the kidney tissue damages induced by cisplatin were greatly reduced in the

L-carnitine pre-treated group (Figure S10, Supporting Information). All these phosphorescence imaging results demonstrate that the chemosensor performance of Ir-OTf is suitable for the activatable imaging modality, holding potential for diagnostic imaging of cisplatin-induced kidney injury in vitro and ex vivo. It is noted that before sacrifice, such a deep tissue (kidney) could not be visualized by the whole-body in vivo imaging owing to a huge interference from the tissue autofluorescence background (Figure S11, Supporting Information). This shows the typical drawback of photoluminescence (PL) imaging inevitably caused by using external photoexcitation, emphasizing the necessity of developing background-free optical modalities.

2.3. Afterglow Nanosensor for $\text{O}_2^{\cdot-}$ Detection

Having confirmed the $\text{O}_2^{\cdot-}$ -responsive sensing behavior of Ir-OTf, a MANS probe was constructed by incorporating Ir-OTf with rubrene in micelles of a triblock copolymer, Pluronic F127 (Scheme 2a). The $\text{O}_2^{\cdot-}$ -activatable afterglow emission is supposed to occur by following the proposed mechanism (Scheme 2b); within the nanosensor space, Ir-OTf senses $\text{O}_2^{\cdot-}$ and the $\text{O}_2^{\cdot-}$ -reacted product (Ir-OH) interplays with rubrene for afterglow initiator-substrate reaction and also as an energy-transferring donor-acceptor pair for harvesting sensing signals into the longer wavelength. Note that the emission of F127-encapsulated Ir-OH and the absorption of F127-encapsulated rubrene are spectrally well-matched to potentiate an efficient energy transfer from Ir-OH to rubrene within MANS



Scheme 2. a) Schematic illustration of MANS. b) Proposed mechanism of superoxide-activatable afterglow luminescence in MANS.

(Figure 3a). Transmission electron microscopy (TEM) and dynamic light scattering (DLS) measurements revealed that the obtained MANS colloids are spherical in shape with a diameter of ≈ 20 nm (Figure 3b) and have a hydrodynamic size distribution of 25 ± 6 nm in water (Figure 3c), respectively.

Afterglow sensing responses of MANS were examined by conducting a sensing reaction with $O_2^{\cdot-}$ and then measuring the afterglow emission in the dark 1 min after pre-excitation with a 448-nm LED lamp for 30 s (Figure 3d). Without exposure to superoxide, MANS exhibited dim and broad-spectrum afterglow luminescence with a peak at 620 nm; however, after reaction with $O_2^{\cdot-}$, it presented much more intense and blue-shifted emission that is similar to the PL spectrum of F127-encapsulated rubrene (Figure 3a), thus suggesting that the afterglow excitation energy is efficiently harvested to the low-bandgap rubrene in the nanostructure of MANS. The $O_2^{\cdot-}$ -activated afterglow signal was shown to be ca. 3.4-fold intensified and long-lasting, which continued to luminesce even 10 min after pre-excitation (Figure 3e and Figure S12, Supporting Information). These results indicate the successful design of MANS for the activatable afterglow detection of $O_2^{\cdot-}$.

The proposed mechanism for the $O_2^{\cdot-}$ -responsive afterglow activation in multifunction-harnessed MANS involves a series of sequential steps (Scheme 2b). First, Ir-OTf reacts selectively with $O_2^{\cdot-}$ to produce optically active Ir-OH in MANS (Step 1). Then, photosensitizing Ir-OH acts as an afterglow initiator

by sensitizing ground-state oxygen (3O_2) into high-energy 1O_2 under pre-excitation at 448 nm (Step 2). The high energy of 1O_2 is stored chemically by oxidizing the co-encapsulated afterglow substrate (rubrene) to form rubrene peroxide (Step 3). The unstable oxidized afterglow substrate degrades slowly and persistently transfers its chemical energy to the remaining rubrene (Step 4) and/or Ir-OH (Step 5) to excite them. The energy collected by phosphorescent Ir-OH is likely harvested to low-bandgap rubrene by the intraparticle energy transfer (Step 6). Eventually, the pre-excitation energy is harvested to excite rubrene that persistently emits long-lasting afterglow even in the absence of the sustained external photoexcitation (Step 7).

To prove the proposed mechanism, a series of experiments were conducted. First, photosensitized 1O_2 production by $O_2^{\cdot-}$ -activated MANS was confirmed using *p*-nitrosodimethylaniline (RNO), a well-known 1O_2 sensor with a specific absorption band at 440 nm which is selectively bleached by 1O_2 , with the aid of singlet oxygen trapper, L-histidine. After photoexcitation with a light-emitting diode (LED) lamp at 448 nm, $O_2^{\cdot-}$ -activated MANS showed a significant decrease in the absorption band of RNO at 440 nm, whereas the RNO bleaching by MANS was much less in the absence of $O_2^{\cdot-}$, demonstrating the enhanced 1O_2 production by $O_2^{\cdot-}$ activation (Figure S13, Supporting Information). To identify the emitter of the apparent afterglow signal from MANS, the PL lifetimes of Ir-OH and Ir-OH + rubrene encapsulated with F127 in PBS (pH 7.4, denoted as Ir-OH NP

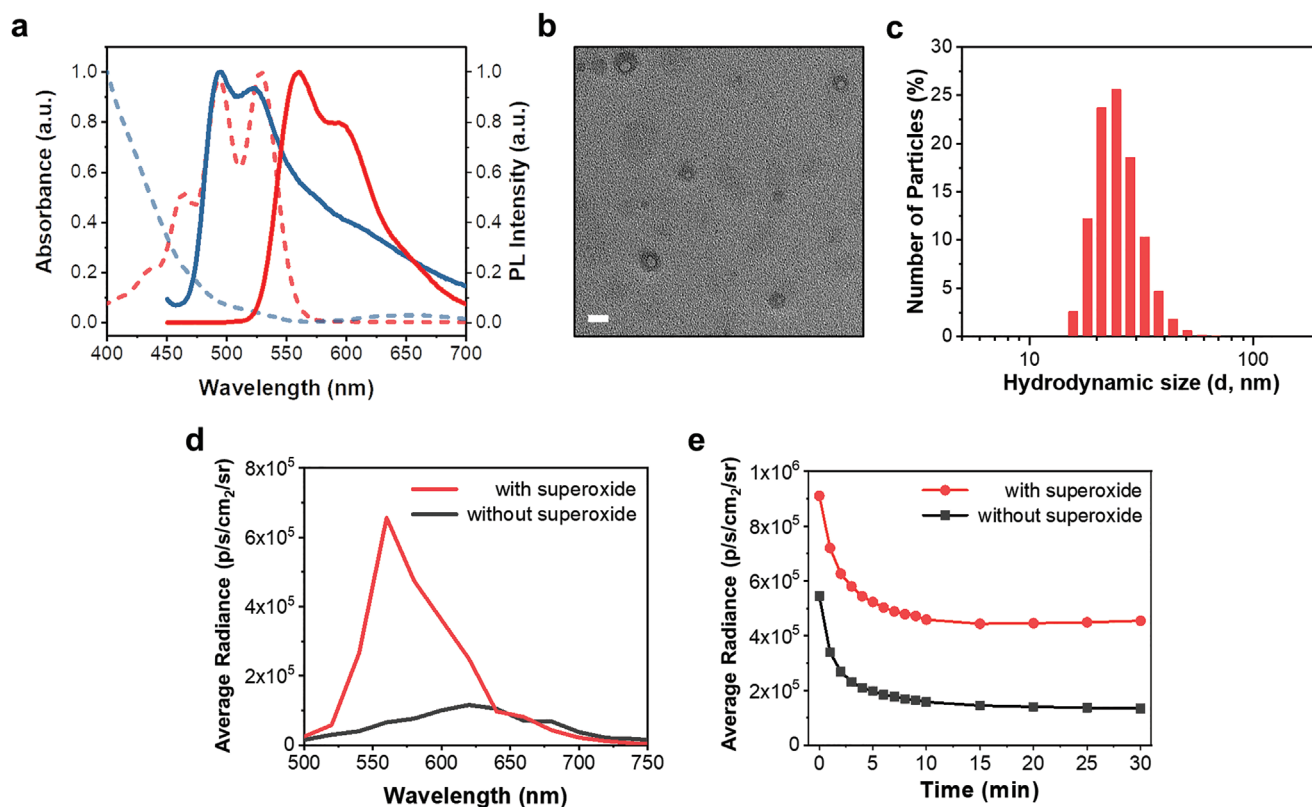


Figure 3. a) Normalized absorption (dash line) and photoluminescence (solid line, λ_{ex} : 420 nm) spectra of Ir-OH (navy) and rubrene (red), each of which was encapsulated with F127 in PBS (pH 7.4). b) Morphology (scale bar: 20 nm) and c) hydrodynamic size distribution of MANS, measured by transmission electron microscopy (TEM) and dynamic light scattering (DLS), respectively. d) Afterglow luminescence spectra and e) time-dependent afterglow radiance profiles (at 560 nm) of MANS with and without $\text{O}_2^{\cdot-}$ reaction in PBS (pH 7.4), measured 1 min after 448-nm LED pre-irradiation for 30 s.

and Ir-OH+Rubrene NP, respectively) were measured using time-correlated single-photon counting (TCSPC) at the emission wavelength of Ir-OH (500 nm) (Figure S14, Supporting Information). The phosphorescent triplet state of Ir-OH NP showed an average lifetime of ≈ 320 ns at 500 nm; while it was considerably shortened to ≈ 170 ns when co-encapsulated with rubrene (Ir-OH + Rubrene NP), indicating the occurrence of resonance energy transfer from the donor (Ir-OH) to the acceptor (rubrene).^[52] This result is in a good agreement with the afterglow spectrum of $\text{O}_2^{\cdot-}$ -activated MANS (Figure 3d) where the donor (Ir-OH) emission at 500 nm is negligible, suggesting that the apparent afterglow luminophore in our superoxide-activatable nanosensor system is rubrene.

2.4. Activatable Afterglow Imaging of AKI In Vivo

Finally, multifunction-harnessed MANS was applied to the background-free “off-to-on” activatable afterglow imaging of AKI in vivo (Figure 4a). The cisplatin-induced AKI mouse models with and without L-carnitine pre-treatment were prepared in the same manner as the above ex vivo phosphorescence imaging experiment, and 2 d after cisplatin treatment, were administered with MANS (210 mg kg^{-1}) intraperitoneally. The dorsal side of each mouse was pre-irradiated with a LED

lamp at 448 nm for 30 s to activate afterglow signaling and then imaged using the IVIS Spectrum imaging system in the absence of photoexcitation. As shown in Figure 4b, the afterglow luminescence from MANS was clearly observed in the injured kidneys of the cisplatin-treated mice with much higher intensity than that from the normal control group. Moreover, the afterglow injury signal was significantly reduced when pretreated with L-carnitine. Indeed, the ex vivo PL imaging revealed that the phosphorescence of MANS-loaded Ir-OTf was turned on only in the cisplatin-treated kidney (Figure 4c). These results demonstrate that the level of $\text{O}_2^{\cdot-}$ was raised by AKI and that the inflammatory response to injury was relieved by L-carnitine, being well accordant to the histological observation (Figure S10, Supporting Information). In this experiment, since L-carnitine was sufficiently treated to reduce the superoxide from acute kidney injury, the results indicate that the amount of superoxide in the kidneys of cisplatin + L-carnitine group was even lower than its normal physiological level in the control group. Therefore, the afterglow luminescence imaging that is free of autofluorescence background revealed an extremely low signal from the mice kidney in cisplatin + L-carnitine group (Figure 4d), well reflecting the effect of L-carnitine. However, in the case of PL measurement in Figure 4c,e, autofluorescence from a biological structure was inevitably involved along with the phosphorescence from the probe. In the control

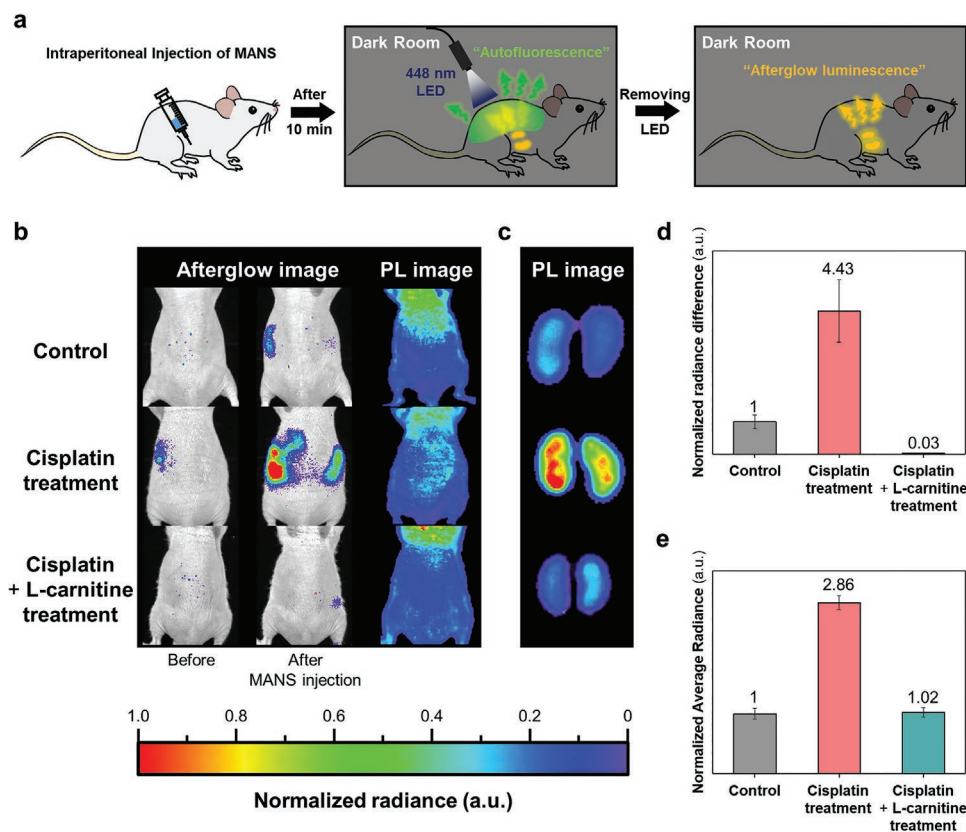


Figure 4. a) Schematic procedure for the afterglow imaging of AKI mouse model after MANS injection, and b–e) the obtained afterglow luminescence and photoluminescence (PL) images along with histograms of the relative luminescence intensities. Mice were pre-injected with PBS, cisplatin (20 mg kg^{-1}), or cisplatin with L-carnitine (500 mg kg^{-1}) 48 h before the intraperitoneal injection of MANS (210 mg kg^{-1}). Before imaging, mice were pre-irradiated with a 448-nm LED (0.6 W cm^{-2}) on the dorsal side for 30 s. b) Afterglow luminescence (1 min after LED pre-irradiation) and PL images of mice. c) Ex vivo PL images of MANS-injected mouse kidneys corresponding to (b) (λ_{ex} : 430 nm, λ_{em} : 540 nm). Histograms of d) relative afterglow radiances from kidneys in vivo in (b) after LED pre-irradiation and e) PL radiances of kidneys ex vivo in (c). The data are presented as mean \pm SEM ($n = 3$).

and cisplatin + L-carnitine groups, both of which have low superoxide concentrations, it is conjectured that the tissue autofluorescence was relatively more dominant than the phosphorescence signal from the MANS probe. Therefore, there was no big difference between the two groups in Figure 4e. Importantly, the in vivo afterglow imaging presented a fairly high signal contrast between injured and normal kidneys (injured-to-normal ratio ≈ 4 ; Figure 4d), which is even higher than that of the ex vivo PL imaging (injured-to-normal ratio ≈ 3 ; Figure 4e). This is in sharp contrast to the in vivo PL imaging where neither kidney injury signals nor injured-to-normal contrasts were observed due to the huge autofluorescence background from the body under photoexcitation (Figure 4b). All these results emphasize the potential of multifunctional-harnessed simple-composition MANS as an “off-to-on” activatable afterglow nanosensor for the background-free diagnostic imaging in vivo.

3. Conclusions

In summary, a superoxide-activatable afterglow nanosensor was developed by integrating two multifunctional components, Ir-OTf and rubrene, into nanoformulation for the afterglow imaging of cisplatin-induced kidney injury in vivo. A

phosphorescent chemosensor Ir-OTf was designed to perform the multiple functions of: 1) superoxide-activatable phosphorescence recovery; and 2) $^1\text{O}_2$ generation under photoexcitation, and it showed excellent sensitivity and selectivity toward superoxide regardless of other reactive oxygen and nitrogen species. By incorporating Ir-OTf with another multifunctional molecule rubrene in F127, two-component afterglow nanosensor system (MANS) could be simply achieved. In MANS, Ir-OTf was demonstrated to act as a superoxide-responsive afterglow initiator and an afterglow relay unit, and it was also confirmed that rubrene can play dual-functional roles as an afterglow substrate and a luminophore. MANS showed excellent afterglow luminescence which lasts for periods >11 min after pre-excitation with deep-tissue penetration. Finally, MANS successfully demonstrated potential for in vivo molecular imaging of cisplatin-induced AKI with background-free “off-to-on” activatable afterglow signals that is selectively generated in response to superoxide overproduced in the injured kidney.

4. Experimental Section

Materials: All chemicals were purchased from commercial suppliers (Sigma-Aldrich, Tokyo Chemical Industry, etc.) and used without further purification.

Characterization: High-resolution mass spectra (HRMS) were collected using Waters Synapt G2 liquid HDMS, and nuclear magnetic resonance (NMR) spectra were recorded using Bruker-400 with tetramethylsilane (TMS) as the internal standard. Transmission electron microscopy (TEM) images were obtained from FEI Tecnai G² F20 at 200 kV. Hydrodynamic size of nanoparticles was determined by dynamic light scattering (DLS) measurement using Zetasizer Nano ZS (Malvern, UK). UV–vis absorption was measured using a Cary 300 UV–vis spectrophotometer and photoluminescence (PL) measurements were conducted using a QuantaMaster 40 (QM-40) spectrophotometer at room temperature with a 1×1 cm standard quartz cuvette. Phosphorescence decay times were recorded by time-correlated single-photon counting (TCSPC) using a Horiba-Jobin Yvon system with a time resolution of about 100 ps. The in vitro phosphorescent images were acquired using LEICA DMI300B equipped with a Nuance FX multispectral imaging system (CRI, USA). The in vivo and ex vivo afterglow luminescence measurements were carried out using an IVIS Spectrum imaging system (Caliper, USA).

Synthesis of Ir-OH: Dichlorotetrakis(2-(2-pyridinyl)phenyl) diiridium(III) (Ir(ppy)₂Cl)₂ and 4,4'-dihydroxy-2,2'-bipyridine (bpy(OH)₂) were synthesized according to reported procedures.^[53] 0.38 g of bpy(OH)₂ was added to a solution of [Ir(ppy)₂Cl]₂ (0.535 g, 0.5 mmol) in 50 mL of dichloromethane/methanol (DCM/MeOH = 3/2, v/v) and the reaction mixture was refluxed for 24 h. Upon completion, the reaction mixture was cooled to room temperature and filtered to remove any starting materials. The filtrated product was then concentrated to dryness using a rotary evaporator and dissolved in 1 mL of DCM/MeOH (2/4, v/v). Upon addition of an excess amount of ether into the solution, yellow precipitates were obtained which was then filtered and washed with ether to give Ir-OH as a yellow solid. Yield: 80%. HRMS (ESI[−], m/z): [M−2H][−] calcd for C₃₂H₂₄IrN₄O₂, 687.1505; found, 687.1059.

Synthesis of Ir-OTf: 200 μL of triethylamine was added to a solution of Ir-OH (0.362 g, 0.5 mmol) in 50 mL of dry DCM and the reaction was stirred at room temperature under argon for 10 min, after which 600 μL of trifluoromethanesulfonic anhydride was added and the reaction mixture was stirred at room temperature for 8 h. Upon completion, the reaction mixture was washed with brine and the organic layer was separated and dried using Mg₂SO₄. The solvent was then evaporated and the solid was dissolved in MeOH. Excess of sodium perchlorate was then added to the solution to yield an orange precipitate, which was then filtered and washed with excess of water and dried in vacuum to give the Ir-OTf as an orange solid. Yield: 65%. ¹H NMR (400 MHz, DMSO-d₆): δ 6.27 (dd, 2H), 6.97 (m, 2H), 7.23 (m, 2H), 7.34 (d, 1H), 7.66 (d, 1H), 7.73 (d, 1H), 7.84 (d, 1H), 8.98 (m, 4H), 8.06 (d, 2H), 8.34 (t, 2H), 8.50 (s, 1H) 9.35 (s, 1H). Elemental analysis of C₃₄H₂₂F₆IrN₄O₆S₂: C 42%, H 2.33%, F 11.9%, Ir 20.17%, N 5.88%, O₂ 10.07%. HRMS (ESI[−], m/z): [M][−] calcd for C₃₄H₂₂F₆IrN₄O₆S₂, 953.0514; found, 953.0513.

Fabrication of MANS: 0.5 mg of Ir-OTf, 0.5 mg of rubrene, and 20 mg of Pluronic F127 were dissolved in 100 μL of tetrahydrofuran (THF) to afford a clear solution, and the mixture was then sonicated. While sonicating, 1 mL of distilled water was added to the mixture and it was further sonicated for 3 min. After this, THF was evaporated using a nitrogen gas blower and the volume of the solution was adjusted to 1 mL using distilled water.

Chemosensor Response of Ir-OTf to ROS: To measure the photophysical properties, the stock solution of Ir-OTf (1 mM) in dimethyl sulfoxide (DMSO) was prepared and further diluted to 10 μM in phosphate-buffered saline (PBS, pH 7.4). ROS used were prepared according to reported procedures.^[54] O₂[−] was prepared by KO₂ dissolved in DMSO containing 0.2 M 18-crown-6 ether. ¹O₂ solution was prepared by NaClO-H₂O₂ system, and ·OH solution was prepared by Fenton reaction of Fe²⁺ with H₂O₂. H₂O₂, ONOO[−], H₂S, ·OCl, Cys, GSH, and NO solution were prepared by dissolving the commercial chemicals H₂O₂, NaONOO, Na₂S, NaClO, Cys, GSH, and sodium nitroprusside in PBS (pH 7.4), respectively. 10 μM of each ROS and different concentrations of superoxide (final concentration: 0–50 μM) in PBS were added to the solution of Ir-OTf (final concentration: 5 μM) in PBS at room temperature. Then, the UV–vis and phosphorescent spectra of the

solution were then recorded at room temperature upon excitation at 420 nm.

Afterglow Sensing Response of MANS to Superoxide: The afterglow sensing response of MANS was tested using an IVIS Spectrum imaging system. 80 μL of MANS in distilled water was added into a dark 96 well plate, and 20 μL of KO₂ in PBS (pH 7.4) was added to it. After 10 min, the luminescence of the samples at 560 nm was measured over time 1 min after pre-excitation with a 448-nm LED lamp for 30 s.

Cell Culture: The HEK293 human embryonic kidney cells were obtained from a Korean Cell Line Bank. Cells were cultured in a high glucose Dulbecco's Modified Eagle Medium (DMEM) containing 10% fetal bovine serum (FBS) and 1% antibiotics (100 U mL^{−1} penicillin, 0.1 mg mL^{−1} streptomycin) at 37 °C in a 5% CO₂ incubator.

In Vitro Phosphorescence Imaging of Superoxide: For the microscopy experiment, HEK293 cells were seeded onto a glass-bottom culture dish at a density of 4.0×10⁴ cells per well for 24 h. After 24 h, the medium was removed, and the cells were incubated at 37 °C as follows. The first group was incubated with only Ir-OTf probe (10 μM) for 30 min. The second group was treated with different concentrations of cisplatin (100–1000 μM) for 12 h, and then treated with the probe (10 μM) for 30 min. The third group was treated with cisplatin (1000 μM) and different concentrations of L-carnitine (100–1000 μM) for 12 h, followed by the probe treatment (10 μM) for 30 min. All cells were washed twice with PBS before treatment and imaging. Then, the treated cells were imaged with a filter set for the phosphorescence of the recovered Ir-OH (λ_{ex}: 425 nm; λ_{em}: 500–600 nm). ImageJ software was used to determine the phosphorescence intensities of Ir-OTf in cells.

In Vivo Imaging of Cisplatin-Induced Kidney Injury in Mice: The animal studies have been approved by the animal care and use committee of Korea Institute of Science and Technology (KIST), and all handling of mice was performed in accordance with the institutional regulations (KIST-2020-019). To induce the AKI, BALB/c nude mice (male, 5 weeks old, Orient Bio Inc., Korea) were intraperitoneally injected with 200 μL of 20 mg kg^{−1} of cisplatin in 0.9% saline (cisplatin group) or blank saline only (control group), and then subjected to imaging probe injection after 48 h. For the pretreatment with L-carnitine (L-carnitine group), mice received L-carnitine (500 mg kg^{−1}) in 0.9% saline peritoneally 24 h before the injection of cisplatin (20 mg kg^{−1}). These three groups received Ir-OTf (0.95 mg kg^{−1}) intravenously or MANS (210 mg kg^{−1}) intraperitoneally 48 h after the treatment with cisplatin or blank saline, and then subjected to IVIS imaging. For afterglow imaging, the MANS-treated groups were pre-irradiated with a 448-nm LED (0.6 W cm^{−2}) on the dorsal side for 30 s before imaging. For the histopathological studies, liver and kidney tissues were fixed in 10% neutral buffered formalin after harvesting them from the mice.

Statistical Analysis: All experimental data are represented as mean ± standard error of the mean (SEM) (n ≥ 3).

Supporting Information

Supporting Information is available from the Wiley Online Library or from the author.

Acknowledgements

T.F.A., H.C., and J.Y. contributed equally to this work. This work was supported by grants from the National Research Foundation of Korea (NRF-2017M3A9D8029942, NRF-2021R1A2C2005418, and NRF-2021R1A2C4002030), the Korea Health Industry Development Institute (HW20C2104), and the KIST intramural program.

Conflict of Interest

The authors declare no conflict of interest.

Data Availability Statement

The data that support the findings of this study are available on request from the corresponding author. The data are not publicly available due to privacy or ethical restrictions.

Keywords

afterglow, multifunctional iridium complexes, phosphorescence, superoxide-activatable afterglow systems

Received: January 12, 2022

Revised: March 8, 2022

Published online: March 22, 2022

- [1] S. Ohkuma, B. Poole, *Proc. Natl. Acad. Sci. USA* **1978**, *75*, 3327.
- [2] Y. Gabe, Y. Urano, K. Kikuchi, H. Kojima, T. Nagano, *J. Am. Chem. Soc.* **2004**, *126*, 3357.
- [3] M. Kamiya, H. Kobayashi, Y. Hama, Y. Koyama, M. Bernardo, T. Nagano, P. L. Choyke, Y. Urano, *J. Am. Chem. Soc.* **2007**, *129*, 3918.
- [4] G. Y. Liu, S. C. Zhang, Y. H. Shi, X. Y. Huang, Y. Y. Tang, P. Chen, W. L. Si, W. Huang, X. C. Dong, *Adv. Funct. Mater.* **2018**, *28*, 1804317.
- [5] J. Wang, J. L. Li, J. N. Yu, H. W. Zhang, B. B. Zhang, *ACS Nano* **2018**, *12*, 4246.
- [6] Y. Feng, R. Liu, L. C. Zhang, Z. Y. Li, Y. Y. Su, Y. Lv, *ACS Appl. Mater. Interfaces* **2019**, *11*, 44978.
- [7] Z. J. Li, N. Yu, J. J. Zhou, Y. Li, Y. W. Zhang, L. Huang, K. Huang, Y. Zhao, S. Kelmar, J. Y. Yang, G. Han, *Adv. Mater.* **2020**, *32*, 2003881.
- [8] S. Xu, R. F. Chen, C. Zheng, W. Huang, *Adv. Mater.* **2016**, *28*, 9920.
- [9] X. Zhen, Y. Tao, Z. F. An, P. Chen, C. J. Xu, R. F. Chen, W. Huang, K. Y. Pu, *Adv. Mater.* **2017**, *29*, 1606665.
- [10] Q. X. Dang, Y. Y. Jiang, J. F. Wang, J. Q. Wang, Q. H. Zhang, M. K. Zhang, S. M. Luo, Y. J. Xie, K. Y. Pu, Q. Q. Li, Z. Li, *Adv. Mater.* **2020**, *32*, 2006752.
- [11] Y. Xu, W. T. Yang, D. F. Yao, K. X. Bian, W. W. Zeng, K. Liu, D. B. Wang, B. B. Zhang, *Chem. Sci.* **2020**, *11*, 419.
- [12] Q. Q. Miao, C. Xie, X. Zhen, Y. Lyu, H. W. Duan, X. G. Liu, J. V. Jokerst, K. Y. Pu, *Nat. Biotechnol.* **2017**, *35*, 1102.
- [13] D. Cui, C. Xie, J. C. Li, Y. Lyu, K. Y. Pu, *Adv. Healthcare Mater.* **2018**, *7*, 1800329.
- [14] Y. Y. Jiang, J. G. Huang, X. Zhen, Z. L. Zeng, J. C. Li, C. Xie, Q. Q. Miao, J. Chen, P. Chen, K. Y. Pu, *Nat. Commun.* **2019**, *10*, 2064.
- [15] X. Ni, X. Y. Zhang, X. C. Duan, H. L. Zheng, X. S. Xue, D. Ding, *Nano Lett.* **2019**, *19*, 318.
- [16] L. Y. Wu, Y. Ishigaki, Y. X. Hu, K. Sugimoto, W. H. Zeng, T. Harimoto, Y. D. Sun, J. He, T. Suzuki, X. Q. Jiang, H. Y. Chen, D. J. Ye, *Nat. Commun.* **2020**, *11*, 446.
- [17] C. Xie, X. Zhen, Q. Q. Miao, Y. Lyu, K. Y. Pu, *Adv. Mater.* **2018**, *30*, 1801331.
- [18] X. Zhen, C. Xie, K. Y. Pu, *Angew. Chem., Int. Ed. Engl.* **2018**, *57*, 4002.
- [19] H. L. Ma, Q. Peng, Z. F. An, W. Huang, Z. G. Shuai, *J. Am. Chem. Soc.* **2019**, *141*, 1010.
- [20] S. Z. Cai, H. L. Ma, H. F. Shi, H. Wang, X. Wang, L. X. Xiao, W. P. Ye, K. W. Huang, X. D. Cao, N. Gan, C. Q. Ma, M. X. Gu, L. L. Song, H. Xu, Y. T. Tao, C. F. Zhang, W. Yao, Z. F. An, W. Huang, *Nat. Commun.* **2019**, *10*, 4247.
- [21] Q. Peng, H. L. Ma, Z. G. Shuai, *Acc. Chem. Res.* **2021**, *54*, 940.
- [22] J. X. Wang, Y. G. Fang, C. X. Li, L. Y. Niu, W. H. Fang, G. L. Cui, Q. Z. Yang, *Angew. Chem., Int. Ed. Engl.* **2020**, *59*, 10118.
- [23] S. Hirata, M. Vacha, *Adv. Opt. Mater.* **2017**, *5*, 1600996.
- [24] K. Jiang, Y. H. Wang, Z. J. Li, H. W. Lin, *Mater. Chem. Front.* **2020**, *4*, 386.
- [25] F. Y. Zhang, X. W. Liang, W. Z. Zhang, Y. L. Wang, H. L. Wang, Y. H. Mohammed, B. Song, R. Zhang, J. L. Yuan, *Biosens. Bioelectron.* **2017**, *87*, 1005.
- [26] T. Hirayama, G. C. Van de Bittner, L. W. Gray, S. Lutsenko, C. J. Chang, *Proc. Natl. Acad. Sci. USA* **2012**, *109*, 2228.
- [27] Q. Zhao, C. H. Huang, F. Y. Li, *Chem. Soc. Rev.* **2011**, *40*, 2508.
- [28] B. J. Powell, *Coord. Chem. Rev.* **2015**, *295*, 46.
- [29] C. Ulbricht, B. Beyer, C. Friebe, A. Winter, U. S. Schubert, *Adv. Mater.* **2009**, *21*, 4418.
- [30] K. C. Tang, K. L. Liu, I. C. Chen, *Chem. Phys. Lett.* **2004**, *386*, 437.
- [31] S. Tobita, T. Yoshihara, *Curr. Opin. Chem. Biol.* **2016**, *33*, 39.
- [32] Z. H. Yan, J. Y. Wang, Y. X. Zhang, S. C. Zhang, J. Qiao, X. R. Zhang, *Chem. Commun.* **2018**, *54*, 9027.
- [33] Z. B. Du, R. Zhang, B. Song, W. Z. Zhang, Y. L. Wang, J. P. Liu, C. L. Liu, Z. P. Xu, J. L. Yuan, *Chem. - Eur. J.* **2019**, *25*, 1498.
- [34] K. Vellaisamy, G. D. Li, W. H. Wang, C. H. Leung, D. L. Ma, *Chem. Sci.* **2018**, *9*, 8171.
- [35] W. J. Xu, S. J. Liu, H. B. Sun, X. Y. Zhao, Q. Zhao, S. Sun, S. Cheng, T. C. Ma, L. X. Zhou, W. Huang, *J. Mater. Chem.* **2011**, *21*, 7572.
- [36] L. Q. Xiong, Q. Zhao, H. L. Chen, Y. B. Wu, Z. S. Dong, Z. G. Zhou, F. Y. Li, *Inorg. Chem.* **2010**, *49*, 6402.
- [37] J. B. Liu, C. Yang, C. N. Ko, V. Kasipandi, B. R. Yang, M. Y. Lee, C. H. Leung, D. L. Ma, *Sens. Actuators, B* **2017**, *243*, 971.
- [38] Y. Tang, H. R. Yang, H. B. Sun, S. J. Liu, J. X. Wang, Q. Zhao, X. M. Liu, W. J. Xu, S. B. Li, W. Huang, *Chem. - Eur. J.* **2013**, *19*, 1311.
- [39] J. S. Nam, M. G. Kang, J. Kang, S. Y. Park, S. J. C. Lee, H. T. Kim, J. K. Seo, O. H. Kwon, M. H. Lim, H. W. Rhee, T. H. Kwon, *J. Am. Chem. Soc.* **2016**, *138*, 10968.
- [40] J. Kang, J. S. Nam, H. J. Lee, G. Nam, H. W. Rhee, T. H. Kwon, M. H. Lim, *Chem. Sci.* **2019**, *10*, 6855.
- [41] J. J. Hu, N. K. Wong, S. Ye, X. M. Chen, M. Y. Lu, A. Q. Zhao, Y. H. Guo, A. C. H. Ma, A. Y. H. Leung, J. G. Shen, D. Yang, *J. Am. Chem. Soc.* **2015**, *137*, 6837.
- [42] S. Lee, W. S. Han, *Inorg. Chem. Front.* **2020**, *7*, 2396.
- [43] P. Pacher, J. S. Beckman, L. Liaudet, *Physiol. Rev.* **2007**, *87*, 315.
- [44] M. Perse, Z. Veceric-Haler, *Biomed. Res. Int.* **2018**, *2018*, 1462802.
- [45] S. S. Motwani, G. M. McMahon, B. D. Humphreys, A. H. Partridge, S. S. Waikar, G. C. Curhan, *J. Clin. Oncol.* **2018**, *36*, 682.
- [46] Z. X. Tang, B. Song, W. Z. Zhang, L. Y. Guo, J. L. Yuan, *Anal. Chem.* **2019**, *91*, 14019.
- [47] Y. Lv, D. Cheng, D. D. Su, M. Chen, B. C. Yin, L. Yuan, X. B. Zhang, *Chem. Sci.* **2018**, *9*, 7606.
- [48] J. Zhang, P. L. Goering, P. Espandiar, M. Shaw, J. V. Bonventre, V. S. Vaidya, R. P. Brown, J. Keenan, C. G. Kilty, N. Sadrieh, J. P. Hanig, *Toxicol. Pathol.* **2009**, *37*, 629.
- [49] E. B. Behling, M. C. Sendao, H. D. C. Francescato, L. M. G. Antunes, R. S. Costa, M. D. P. Bianchi, *Pharmacol. Rep.* **2006**, *58*, 526.
- [50] M. Matera, G. Bellinghieri, G. Costantino, D. Santoro, M. Calvani, V. Savica, *J. Renal Nutr.* **2003**, *13*, 2.
- [51] K. Cayir, A. Karadeniz, A. Yildirim, Y. Kalkan, A. Karakoc, M. Keles, S. B. Tekin, *Cent. Eur. J. Med.* **2009**, *4*, 184.
- [52] P. R. Selvin, T. M. Rana, J. E. Hearst, *J. Am. Chem. Soc.* **1994**, *116*, 6029.
- [53] T. F. Anjong, G. Kim, H. Y. Jang, J. Yoon, J. Kim, *New J. Chem.* **2017**, *41*, 377.
- [54] X. Y. Gao, G. X. Feng, P. N. Manghnani, F. Hu, N. Jiang, J. Z. Liu, B. Liu, J. Z. Sun, B. Z. Tang, *Chem. Commun.* **2017**, *53*, 1653.